

The effect of high dose rate gamma irradiation on the curing of
CaO-FexOy-SiO₂ slag based inorganic polymers: Mechanical and
microstructural analysis

Peer-reviewed author version

MAST, Bram; Cambriani, Andrea; Douvalis, Alexios P.; Pontikes, Yiannis;
SCHROEYERS, Wouter; VANDOREN, Bram & SCHREURS, Sonja (2020) The
effect of high dose rate gamma irradiation on the curing of CaO-FexOy-SiO₂ slag
based inorganic polymers: Mechanical and microstructural analysis. In: Journal of
nuclear materials, 539 (Art N° 152237).

DOI: 10.1016/j.jnucmat.2020.152237

Handle: <http://hdl.handle.net/1942/31456>

The effect of high dose rate gamma irradiation on the curing of CaO-FeO_x-SiO₂ slag based inorganic polymers: Mechanical and microstructural analysis.

Bram Mast^{a*}, Andrea Cambriani^b, Alexios P. Douvalis^c, Yiannis Pontikes^d, Wouter Schroeyers^a, Bram Vandoren^e, Sonja Schreurs^{a**}

^a Hasselt University, CMK, NuTeC, Nuclear Technology - Faculty of Engineering Technology, Agoralaan Building H, B-3590 Diepenbeek, Belgium

^b European Commission, Joint Research Centre, P.O. Box 2340, D-76125 Karlsruhe, Germany

^c University of Ioannina, Department of Physics, 45110 Ioannina, Greece

^d KU Leuven, Department of Materials Engineering, Kasteelpark Arenberg 44, 3001 Heverlee, Belgium

^e Hasselt University, CERG, Faculty of Engineering Technology, Agoralaan Building H, B-3590 Diepenbeek, Belgium

* Main Author, E-mail: bram.mast@uhasselt.be

**Corresponding Author: sonja.schreurs@uhasselt.be

Keywords:

Alkali Activated Materials, Fe-rich inorganic polymers, gamma irradiation, mechanical and microstructural changes, radiation-induced strengthening, radiation-induced iron oxidation

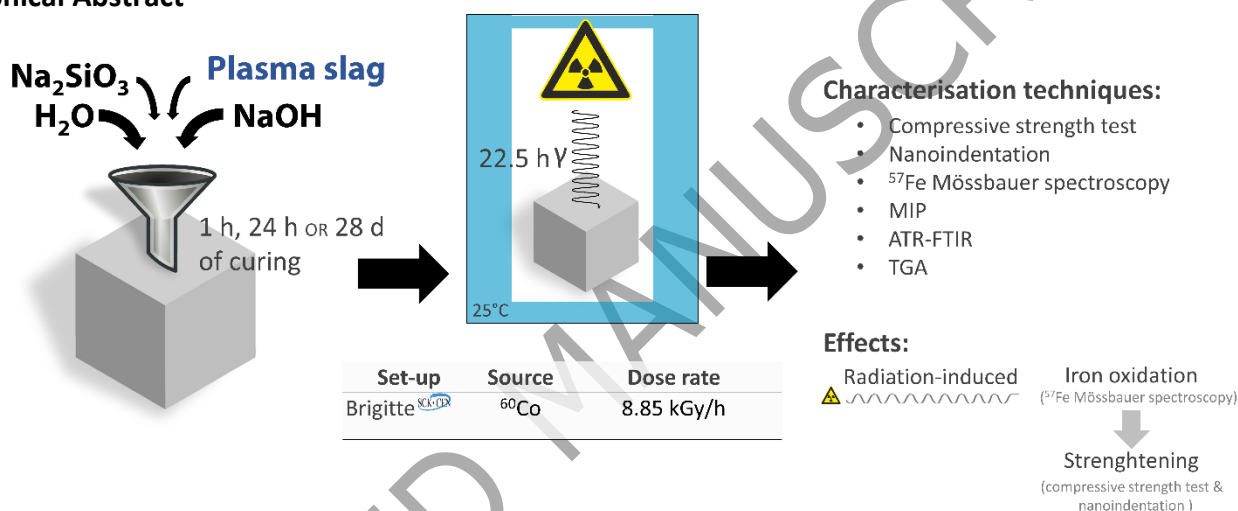
Declarations of interest: none

Abstract

In search for alternative cementitious materials for radioactive waste encapsulation, geopolymers and inorganic polymers (IPs) have received wide attention. Moreover, Fe-rich IPs offer an interesting alternative to high density concretes for use in radiation shielding applications. Materials can however be altered when subjected to ionizing radiation, creating the necessity to evaluate the material's behaviour under irradiation conditions. In this study the effect of high dose rate (8.85 kGy/h) gamma irradiation is investigated on CaO-FeO_x-SiO₂ slag-based IPs. Samples with different curing times (1 h, 24 h and 28 days) prior to the irradiation were irradiated to a dose of 200 kGy using a ⁶⁰Co source.

The effect of gamma radiation is observed to be highly dependent on the curing time prior to irradiation. 28 days cured samples are found to be resistant to the irradiation for the dose(rate) and properties tested without any significant change in strength, indentation characteristics, porosity and Fe³⁺ content. The IPs studied show a different behaviour when irradiated immediately after casting or after 24 h of curing. It is therefore thought that the mechanism behind the effect of irradiation is different for the non-hardened samples compared to hardened samples. For the 1 hour cured samples prior to irradiation multiple effects were observed: an increase of the compressive strength by a factor 2.20, a decrease in hardness of the binder by a factor of 0.73, a lower Young's-modulus of the binder by a factor of 0.67, a decrease of creep in time for the binder by a factor of 0.72, a decrease in porosity by a factor of 0.92 and an increase of the Fe³⁺/ΣFe ratio by a factor of 1.95.

Graphical Abstract



Highlights

- Iron-rich slag-based IPs were irradiated with a 8.85 kGy/h ⁶⁰Co source.
- The curing time before irradiation affects the material's response.
- We observed strengthening of IPs associated to radiation-induced iron oxidation.

Abbreviations and symbols:

A_c	Contact area
ATR-FTIR	Attenuated Total Reflection Fourier-transform Infrared Spectroscopy
C	Creep modulus
C_{IT}	Normalised indentation creep parameter
E_m	Indentation elastic modulus
F_{max}	Maximum indentation load
H	Hardness
h_0	Initial indentation depth
h_a	Contact perimeter of indenter
h_c	Penetration depth
h_r	Residual impression
h_{max}	Maximum indentation depth
IAEA	International Atomic Energy Agency
IPs	Inorganic Polymers
IRR	Irradiated
IS	Isomeric Shift
$L(t)$	Creep function
MIP	Mercury Intrusion Porosimetry
OPC	Ordinary Portland Cement
PS	Plasma Slag
PSD	Pore Size Distribution
QS	Quadrupole Splitting
RAA	Relative Absorption Area
REF	Reference (non-irradiated)
RT	Room Temperature
S	Stiffness
SEM	Scanning Electron Microscope
TGA	Thermogravimetric Analysis

1 Introduction

In search for alternative cementitious materials for radiation shielding and radioactive waste encapsulation, geopolymers and alkali activated materials have received wide attention [1], [2], [3]. These materials are considered promising due to (i) their excellent performance characteristics and (ii) because they can be synthesised from residue materials. Inorganic polymers (IPs) is the class of inorganic binders which can be formed through the alkali activation of a calcium silicate source comparable to the conventional clinkers, an aluminosilicate source, such as kaolinite and fly ash, or a ferrosilicate source, such as slags from the non-ferrous metal industry.

Plasma slag (PS) from urban solid waste gasification can be considered as an industrial by-product containing a Fe-rich glass fraction which can be valorised through polymer cement/block production [4]. A number of publications can be found in literature using PS of different compositions as a precursor material for IPs [5]–[10]. The chemistry of the slag however influences the properties of the final IP, and thus fluctuations should be limited [11]. Machiels et al. (2016) [7] compared the compositional data of different freshly produced ashes to predict its compositional variation related to the source material, geographical origin and applied pre-concentration method. It was found that most of the samples had a chemistry close to ground granulated blast-furnace slag (GGBFS) and Ca-rich fly ash. Future work however has to focus on the identification of an optimal precursor chemistry which allows the slag producers to harmonise the composition of the non-ferrous metallurgy slags [11].

Fe-rich IPs offer an interesting alternative to high density concretes for use in radiation shielding applications, from an economical point of view, since the slags necessary to produce IPs are cheaper than the minerals used in high density concretes [12]. IPs are also interesting candidates for the conditioning of certain radioactive waste streams due to (i) the absence of portlandite, (ii) the low water content and (iii) the high alkalinity [3]. (i) Portlandite has weak immobilization capacities. Moreover, it is unwanted for the immobilization of reactive metals since NaF cannot be added in the presence of portlandite to decrease the metallic corrosion and corresponding dihydrogen production. (ii) A low water content is desired to limit the radiolytic hydrogen yield, since radiolytic dehydration is one of the most important effects which can cause damage in cementitious materials. Moreover, radiolytic dihydrogen formation should be limited to avoid internal pressure build up. For IPs, however, this is expected to be of less concern, since literature indicates that the apparent H_2 yield for IPs is below that of ordinary Portland cement-based samples [3]. The H_2 yield is though affected by the presence of salts and ionic species in the pore water. Since salts as $Ca(OH)_2$

can interact with radiolytic H_2O_2 , they can increase the hydrogen gas production [13]. As more H_2O_2 is consumed, less is available for the oxidation of hydrogen to water [13]. Ionic species and nitrate salts on the other hand can decrease the H_2 yield as they interact with hydrated electrons and hydrogen atoms and thus avoid recombination to H_2 . Moreover, this effect can increase when the ion concentration in the pore solution increases as dehydration progresses. (iii) High alkalinity is desired since high pH insolubilizes many metals and radioelements such as ^{137}Cs and protects safety barriers from corrosion. [3]

Materials used for radioactive waste encapsulation are subjected to different dose rates, with a maximum immediately after waste conditioning/emplacement and a decrease over time as a result of radioactive decay. The dose rate highly depends on the type of waste and the position of the material in the conditioning matrix. According to the Belgian waste management system, the gamma dose rate for waste conditioning can vary from a minimum of 5 mGy/h at contact dose for the low-level wastes to a maximum of 23 Gy/h close to the radioactive source for vitrified high-level waste [14]–[16]. Peak gamma dose rates for high-level waste disposal varying from 35 mGy/h to 10 Gy/h have been reported by Bennet et al. (2008) [17]. Much higher dose rates are applicable in nuclear reactors at the concrete interface. A flux of $\pm 3 \cdot 10^9$ rad/s ($\approx 1 \cdot 10^{11}$ Gy/h) has been reported for a three-loop pressurised water reactor [18], [19].

The detrimental effects of gamma radiation on OPC-based matrices have been studied extensively [20]–[27]. However, less studies can be found examining the effect of gamma radiation on IPs [28]–[36]. Most of these studies focus on metakaolin-based geopolymers. In literature, radiation-induced strengthening is reported for metakaolin Na-geopolymers by Lambertin et al. (2013) [31] and for iron-rich IPs by Mast et al. (2019) [35]. A possible explanation for this strengthening could be a change in the pore size distribution [35]–[37]. The increased strength as a result of irradiation can also be related to the growth of carbonates e.g. CaCO_3 or Na_2CO_3 in the microcracks and pores [24], [38]. Or, in the case of iron-rich IPs, the strength increase can be related to the radiolytic effect on the different oxidation states of iron, which also determines the strength of non-irradiated IPs [8], [10].

In literature, also altered creep properties of cementitious materials as a result of gamma irradiation are reported [27]. Hilloulin et al. (2018) [27] used microindentations with a maximum load of 2000 mN to characterise the creep properties of the individual phases of fully hardened mortar samples after irradiation. They found a significant increase (+ 17%) in cement paste creep modulus after an exposure of 257 kGy at 510 Gy/h [27]. The creep modulus increase is corresponding to a slight increase in indentation hardness. The indentation modulus was not significantly affected. No results have yet been found in literature describing the effect of gamma irradiation on the micromechanical properties of IPs.

This research focusses on a general description of the effects of gamma irradiation on inorganic polymers, proposing a mechanism to describe the strength increase for irradiated samples [35]. The effect of high dose rate (8.85 kGy/h) gamma irradiation is investigated on iron-rich $\text{CaO-FeO}_x\text{-SiO}_2$ slag-based IPs. A high dose rate was applied to increase the irradiation effects and to mimic irradiation effects at the larger timescale. The macro- and micromechanical properties are studied as well as the microstructural characteristics. Compressive strength, indentation modulus, hardness, creep, pore size distribution, water content, carbonate content, and iron oxidation state were evaluated for the irradiated samples and compared to non-irradiated samples. The mix design used in this study should be optimised when focussing on a specific application such as nuclear waste management.

2 Material and methods

2.1. Inorganic polymer

A synthetic plasma slag (Figure 1) with chemical composition as given in Table 1 was produced using bottom ash, iron ore, limestone, and sand to represent a slag often used in non-ferrous metallurgy [7]. The melt was quenched using pressurised water jets and a water tank to obtain a vitrified material with high amount of amorphous phase (> 98 wt.%). The methodology for producing the synthetic slag is described in more detail in Machiels et al. (2016) [7].

The quenched glass was milled using a ball mill until a Blaine value of $(2.68 \pm 0.02) \cdot 10^3 \text{ cm}^2/\text{g}$ according to EN 196-6 [39] before alkali activation. The milled slag, hereafter referred to as precursor, had a density of $(3.094 \pm 0.009) \text{ g/cm}^3$ measured using the Quantachrome Multipycnometer MVP-6DC and a particle size distribution of $D_{10} = (3.87 \pm 0.06) \mu\text{m}$, $D_{50} = (22.3 \pm 0.7) \mu\text{m}$ and $D_{90} = (68 \pm 2) \mu\text{m}$. The chemical composition of the precursor was determined using X-ray fluorescence analysis (Bruker S8 TIGER). High amounts of SiO_2 , FeO , CaO and Al_2O_3 were detected, as can be observed in Table 1.



Figure 1: Photograph of non-milled plasma slag.

Table 1. Chemical composition of synthetic plasma slag (PS) according to XRF. Fe_xO_y is expressed as 92% FeO and 8% Fe_2O_3 .

wt.%	SiO_2	Fe_xO_y	CaO	Al_2O_3	MgO	TiO_2	K_2O	Other
PS	29.2	28.2	26.7	13.4	0.8	0.7	0.6	0.4

The IP pastes were produced by mixing the precursor with a sodium silicate activation solution. The activation solution was a mixture of sodium silicate solution (molar ratio $\text{SiO}_2/\text{Na}_2\text{O} = 3.3$ and 65 wt.% water, supplied by ABCR GmbH), sodium hydroxide pellets (grade 98.8%, supplied by VWR international) and distilled water. An activation solution with molar ratios of $\text{SiO}_2/\text{Na}_2\text{O} = 1.6$ and $\text{H}_2\text{O}/\text{Na}_2\text{O} = 20.0$, was used. 69.54 g of Na_2SiO_3 solution, 8.05 g of NaOH pellets and 22.41 g of distilled water were mixed for 100 g of activation solution. The precursor was mixed with the solution in a solid to liquid ratio of 2.6 g/ml. The binder recipe has been selected as the authors focussed on a design with enough binder phase such as to allow the characterisation of the individual phases via nanoindentation. The binder recipe was also adjusted to have limited reactivity to avoid microcracking, since this would both affect the performance and the nanoindentation results. Moreover, a higher amount of binder phase was preferred to make the impact of the irradiation more pronounced. Irradiation effects in the binder were expected to be of higher importance to the material properties than effects in the unreacted particles.

The paste was cast in a small cubic (25^3 mm^3) or cylindrical ($d = 30 \text{ mm}$, $h = 40 \text{ mm}$) mould and vibrated during 3 minutes at 50 Hz using the Controls 55-C0159/L vibrating table. The samples were cured at a temperature of $(28.8 \pm 0.5)^\circ\text{C}$ and a relative humidity of $(54 \pm 10)\%$ in an environmental chamber for 1 hour, 24 hours or 28 days prior to irradiation. These time intervals are chosen based on the different reaction stages:

- 1 h: minimum time after casing necessary to load the samples in the irradiation cell;
- 24 h: right after the main reaction peak;
- 28 d: stable and fully cured sample.

After 28 d of curing, samples with a bulk density of about 2.5 g/cm^3 were obtained with a microstructure as in Figure 2 (i). Some microcracks as a result of drying shrinkage can be observed. Dimensional changes are reported in a previous study of Mast et al. (2019) [35]. For the non-irradiated samples, volumetric changes up to -5% were observed. As large deformations resulting from shrinkage are undesired for nuclear waste management applications, dimensional stability should be optimised by adapting the synthesis parameters such as precursors' reactivity and curing conditions [40].

Since the final setting time is about 6 hours, the 1 hour hardened samples were still very viscous at the start of the irradiation, while the others were solidified. The IP.1s were irradiated during the dissolution and polymerisation stage, while for the IP.24s the irradiation started when then main reactions (dissolution, reorganisation, gelation and polymerisation) were already finished. A stable and fully cured sample is only obtained after a sufficient curing time. Therefore, also IP.28s were included in the experimental design. The different curing times reflect different material applications in radioactive waste management. For certain barriers, prefabricated and fully hardened materials are preferred, while for others, the material is poured close to the radioactive source(s) causing irradiation during hardening.

2.2. Irradiation set-up

Irradiation was performed at the SCK-CEN BR2 research reactor facility [41]–[43]. The underwater gamma irradiation facility BRIGITTE (Big Radius Installation under Gamma Irradiation for Tailoring and Testing Experiments) was used [41]. Table 2 summarizes the characteristics of the gamma source used in the

169 irradiation test. The irradiation container was surrounded by ten ^{60}Co sources. The irradiation container
 170 was a stainless-steel double-wall (3.5 mm wall thickness) barrel with a 20 cm internal diameter.
 171 Temperature evolution of an IP sample was recorded using a thermocouple which was placed in the centre
 172 of a sample via a 5 mm diameter drilled hole. At the start of the irradiation, a temperature of 25.4 °C was
 173 registered. The temperature however quickly raised to 30.1 °C after 1.5 hour and reached a plateau after
 174 4 hours at 33.6 °C. The irradiation was performed in stagnant atmosphere with the sample container
 175 immersed in a water basin of about 25 °C.

176 **Table 2.** Characteristics of irradiation set-up.

Irradiation facility	Brigitte position B at SCK·CEN MOL
Source	^{60}Co
Decay	$^{60}\text{Co} \rightarrow ^{60}\text{Ni} + e^- + \nu_e + \gamma$
Energy	1.173 MeV, 1.332 MeV
Irradiation time	22.5 h
Time before irradiation	1 h, 24 h or 28 d
Max dose rate	8.85 kGy/h

177

178 The dose-rate for the irradiation was calculated using a dose rate map based on measurements with Harwell
 179 Amber 3042 Dosimeters [44]. To perform the dose-rate mapping, the dosimeters were placed on the central
 180 axis of the container. The dose-rate variation on horizontal planes in the container without samples is \pm
 181 10%. Samples were placed at the position with maximum dose rate of 8.85 kGy/h for 22.5 hours resulting
 182 in a total dose of 200 kGy.

183 Samples were named according to their time before irradiation. The ID's are listed in Table 3. Irradiated
 184 samples were compared to reference samples for which the same procedures were applied as for the
 185 irradiated samples, except for the irradiation itself. No reaction stoppage procedure was applied. The
 186 reference samples were kept at the same ambient conditions as the irradiation samples during and after
 187 irradiation. It is not recommended to compare sample results to other than their reference since manual
 188 operations in the production method of different batches might slightly deviate.

189

Table 3. Sample ID's.

	Reference samples	Irradiated samples
1 hour hardened	IP.1.REF	IP.1.IR
24 hours hardened	IP.24.REF	IP.24.IR
28 day hardened	IP.28.REF	IP.28.IR

190

191 **2.3. Evaluation of irradiation effects**

192 **2.3.1. Macro-mechanical behaviour**

193 Compressive strengths tests were performed to evaluate the mechanical properties of the samples
 194 measuring ([25 x 25] x 20) mm³. The tests were executed in triplicate. Uniaxial tests were performed
 195 according to NBN EN 12390-3 [45] using a Instron 5985 with a compression speed of 1.0 mm/min. The
 196 compressive strength in MPa was calculated as the maximum load at fracture in Newtons divided by the
 197 contact area of the auxiliary plates in mm².

198 **2.3.2. Micro-mechanical behaviour: nanoindentation**

199 Nanoindentation was used to determine the Young's modulus, hardness and creep of the individual
 200 constituents of the IP. The irradiated and non-irradiated samples for nanoindentation were cut plane-
 201 parallel and polished to reduce the surface roughness. The procedure followed, as described in Table 4,
 202 was similar to that of Miller et al. (2008) [46] and Nedeljkovic et al. (2018) [47]. Next a disk of \pm 2 mm
 203 thickness was cut of the cylindrical samples using a water-cooled diamond saw. Finally, the samples were
 204 cleaned in an ultrasonic bath and mounted on a rigid sample holder with little amount of glue.

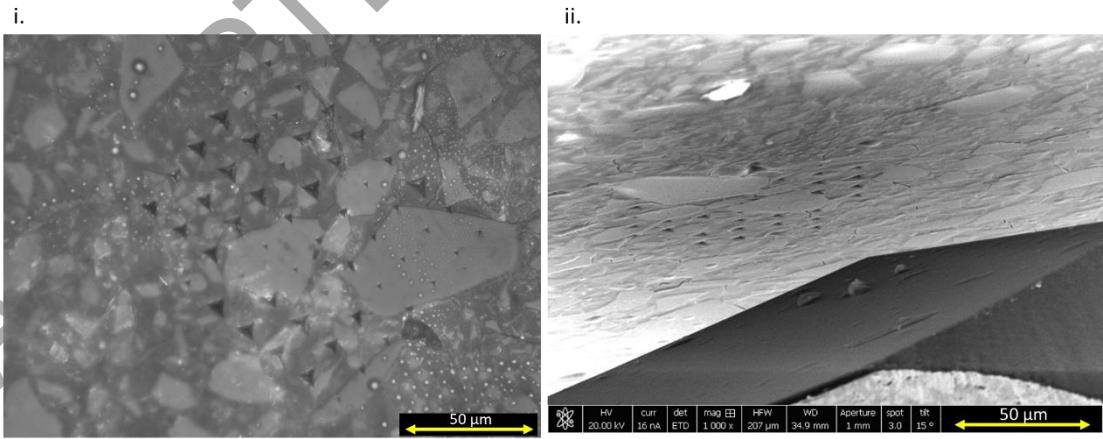
Table 4. Mechanical polishing procedure for nanoindentation tests.

	Polishing Material	Grit (μm)	Duration (min)
1	Sandpaper P-80	201	5
2	Sandpaper P-120	82	5
3	Sandpaper P-320	46.2	5
4	Sandpaper P-800	21.8	10
5	Sandpaper P-1200	15.3	10
6	Silicon carbide P-4000	2.5	15
7	Diamond paste 6	6	20
8	Diamond paste 3	3	20
9	Diamond paste 1	1	30
10	Colloidal Silica Suspension	0.02	> 5 h

206

207 For the evaluation of the mechanical properties of the different phases present in the material, a large grid
208 nanoindentation test was performed using an Alemnis ASA nanoindenter with a Berkovich diamond tip
209 (Figure 2). The indenter was operated in-situ within the SEM vacuum chamber (FIB/SEM Versa 3D from
210 FEI). A grid test was performed executing 50 indents with a spacing of 15 μm between the individual
211 indents (Figure 2). The in-situ configuration was used to select the regions of interest prior to indentation.
212 Light microscopy was used to observe the indentation points after testing and to assign each indent to the
213 corresponding phase (binder or unreacted slag particle). The elastic modulus at the microscale (E_m), the
214 indentation hardness and the indentation creep of each individual phase can be determined from the
215 analysis of the indentation curves. Load controlled indentations were performed. A trapezoidal loading
216 curve was applied with a loading rate of 1 mN/s up to a maximum of 20 mN and an unloading rate of 1
217 mN/s (Figure 3). The maximum load was held constant for 40 seconds, in order to perform a creep analysis.
218 This time interval was chosen long enough to observe creep and short enough to limit thermal drift during
219 this stage. During the unloading, a further step at constant load of 1mN was held for 60 seconds in order
220 to calculate the thermal drift and apply the necessary corrections.

221



222 **Figure 2:** (i) Microstructure of IP.24.REF using light microscope Leica DMI5000M with 53 indentation points (▲) and
223 (ii) Berkovich indenter tip approaching IP.24.REF surface in in-situ SEM. The light grey phases are unreacted slag
224 particles and the dark grey phase is reacted IP binder.

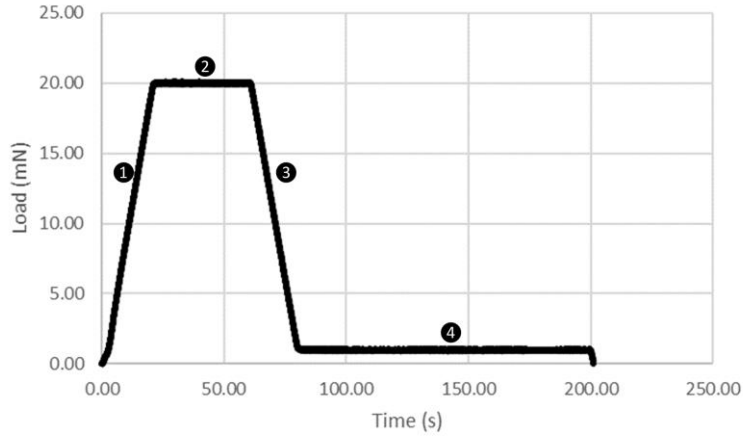


Figure 3: Trapezoidal load curve in function of time.

For the analysis, only two phases were considered: (i) the unreacted slag particles which remain in the paste and (ii) the geopolymer binder phase resulting from the dissolution of slag particles which constitutes the matrix surrounding the unreacted slag particles.

The binder phase is difficult to characterise. When possible, the region for indenting the binder was carefully chosen using the in-situ SEM configuration. Despite the limited footprint of the indent, due to the morphology and distribution of the unreacted particles, it was difficult to select and indent regions where only the binder phase was present. Moreover, it is reasonable to assume that unreacted particles concealed underneath the visible surface of the binder phase randomly contribute to the mechanical response. The binder has therefore to be assumed inherently heterogeneous within the indentation volume probed by the indenter. The probed volume extends well below the maximum indentation depth. A wider scattering of the binder indentation parameters is expected with respect to the unreacted particles' indentations. The indentation load of 20 mN and the corresponding maximum indentation depth represents a good compromise for the selection of a meaningful indentation volume for the binder phase. The resulting indentation depth is small enough to minimise the likelihood of subsurface unreacted particles but not too small to suffer from the uncertainties associated to the actual indenter shape (see further discussion on area function). Indenting an unreacted particle with a load of 20 mN resulted in a maximum indentation depth in the 400 – 500 nm range whereas the corresponding indentation depth for the binder phase was in the 1100 – 1200 nm range, as showed in Figure 4. Both type of indents are therefore clearly distinguishable using light microscope images as shown in Figure 2, where the small indents relate to the unreacted particles.

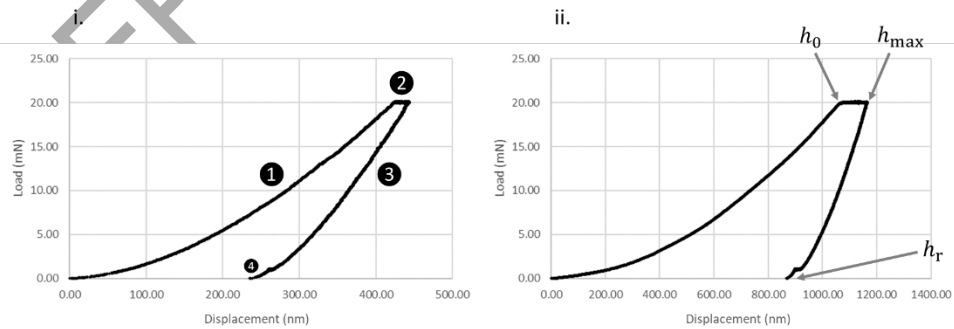


Figure 4: Typical load-displacement curve of indentation on i) unreacted particle and ii) the binder phase.

According to the method proposed by Oliver and Pharr (1992) [48], the material elastic modulus and the indentation hardness can be determined from the elastic unloading part ③ of the load (P)-displacement (h) curve (Figure 4). A Berkovich diamond tip (three-sides pyramid with face angle of 65.27°) was used for the indentations. Following the Oliver and Pharr approach, the contact depth (h_c), as measured from the maximum penetration depth, can be determined from:

$$h_c = h_{\max} - \varepsilon \frac{P_{\max}}{\frac{dP}{dh}}$$

Equation 1

Where $\varepsilon = 0.75$ for a Berkovich indenter and $\frac{dP}{dh}$ is the samples contact stiffness represented by the slope of the tangent to the curve at maximum load. Least square fitting of the unloading section is necessary to calculate the slope. P_{\max} and h_{\max} correspond, respectively, to the maximum load and the maximum indentation depth. Once h_c is known, the area of contact can be calculated from the geometry of the indenter. For an ideal Berkovich indenter the contact area is given by:

$$A_c(h_c) = 24.56 \cdot h_c^2 \quad \text{Equation 2}$$

In order to take into account the real geometry of the indenter tip, i.e. the rounding of the tip which greatly affects the measurements at shallow depths, a correction generally referred to as "area function" is used. The area function is obtained by indenting a fused silica standard with well-known elastic modulus and hardness and it is presented in equation 3.

$$A_c(h_c) = 24.56 \cdot h_c^2 - 7.61 \cdot 10^{-6} \cdot h_c^3 - 1.35 \cdot 10^{-5} \cdot h_c^{1/2} + 8.86 \cdot 10^{-6} \cdot h_c^{1/4} - 1.23 \cdot 10^{-5} \cdot h_c^{1/8} + 1.65 \cdot 10^{-5} \cdot h_c^{1/16} - 1.06 \cdot 10^{-5} \cdot h_c^{1/32} - 4.00 \cdot 10^{-6} \cdot h_c^{1/64} + 5.60 \cdot 10^{-6} \cdot h_c^{1/128} \quad \text{Equation 3}$$

The combined elastic modulus (E^* [GPa]) of the indenter and specimen is then given by

$$E^* = \frac{\frac{dP}{dh} \sqrt{\pi}}{2 \cdot \beta \cdot \sqrt{A_c}} \quad \text{Equation 4}$$

Where β is a correction factor for non-symmetrical indenters equal to 1.034 for a Berkovich tip and A_c is the area of contact described previously. The elastic indentation modulus of the sample (E_m [GPa]) can be derived from the relationship:

$$\frac{1}{E^*} = \frac{1-\nu_{\text{ind}}^2}{E_{\text{ind}}} + \frac{1-\nu^2}{E_m} \quad \text{Equation 5}$$

Where E_{ind} and ν_{ind} are the elastic modulus and the Poisson's ratio of the indenter, with values of $E_{\text{ind}} = 1140$ GPa and $\nu_{\text{ind}} = 0.07$ for the diamond tip. The Poisson's ratio of the sample material, ν , was taken as 0.18.

As for the indentation hardness, (H [GPa]), is given by:

$$H = \frac{P_{\max}}{A_c} \quad \text{Equation 6}$$

The normalised indentation creep parameter C_{IT} [%], was calculated as:

$$C_{IT}(\%) = \frac{h_{\max} - h_0}{h_0} \cdot 100 \quad \text{Equation 7}$$

with h_0 being the initial indentation depth at the start of the indentation creep stage ②. The indentation creep curves were generated using equation 8. The creep function $L(t)$ [Pa^{-1}], also called creep compliance rate $\dot{J}_c(t)$, is fitted with a three parameter logarithmic curve from which the creep parameters (C [GPa] and τ [s]) can be calculated [27], [49], [50]. The higher the value of C , the lower the rate of the creep.

$$\dot{J}_c(t) = L(t) - L(0) = L(t) - \frac{1}{E_m} = \frac{2 \cdot a_u(t) \cdot \Delta h(t)}{F_{\max}} \xrightarrow{\text{logarithmic fit}} \frac{\ln(\frac{t}{\tau} + 1)}{C} \quad \text{Equation 8}$$

In this formula, $\Delta h(t)$ represents the increase in indentation depth during the creep stage. a_u [m] denotes the radius of the equivalent projected contact area of the indenter tip with the specimen surface ($a_u = \sqrt{A_c(h_c)/\pi}$).

The results of the indentation tests of irradiated samples were compared to these of non-irradiated samples. A two-sided two sample t-test at 0.05 level, assuming unequal variances were used to evaluate whether the observed differences are significant.

2.3.3. Other properties – sample preparation

(i) Mercury intrusion porosimetry (MIP) was performed using the Micromeritics Autopore IV 9510 to quantify pores in the 3.6 nm to 100 μm region. Samples of (5 x 5 x 5) mm³ were dried for 48 hours at 30 °C and at atmospheric pressure and next dried for 2 hours at 25 °C down to 10 μm Hg. The samples were tested in the range of 0.01 to 414 MPa. Reproducibility of the analysis was tested by measuring two samples from the same batch. An experimental difference of 0.5% was observed for the porosity of the samples.

300 (ii) Attenuated total reflectance Fourier-transformed infrared (ATR-FTIR) spectroscopy was performed on
 301 IP samples using a Bruker Alpha-P with diamond crystal. Samples were powdered just before analysis using
 302 a Retsch RS200 vibratory disc mill for 10 s. 32 spectra per sample were acquired from 4000 cm^{-1} to 380
 303 cm^{-1} at a resolution of 4 cm^{-1} . The reported spectra are the result of the average of five measurements on
 304 a homogenised powder made of three different samples.

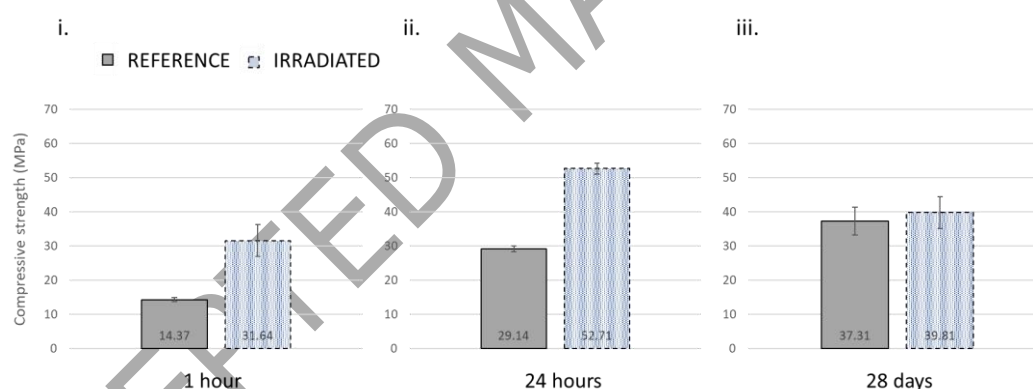
305 (iii) Thermogravimetric analysis (TGA 550 - TA instruments) of the samples was carried out from 20 °C to
 306 800 °C with a heating rate of 10 °C/min in a nitrogen atmosphere. The mass was measured up to 10^{-6} g
 307 precision. Samples were powdered just before analysis using a Retsch RS200 vibratory disc mill for 10 s.

308 (iv) ^{57}Fe Mössbauer spectroscopy measurements were performed to investigate the state and the
 309 environment of the Fe atoms in irradiated and reference samples. Samples were powdered manually to a
 310 fine powder and pressed into the sample holder right before measurement. Gamma rays from a ^{57}Co source
 311 in a Rh matrix was used. The samples were measured at room temperature (RT, 300 K) in transmission
 312 geometry on a constant acceleration spectrometer. Calibration of the spectrometer was performed using
 313 $\alpha\text{-Fe}$ at 300 K. The isomer shift (IS) values are reported relative to $\alpha\text{-Fe}$ at RT. The IMSG software was
 314 used to fit the data [51].

315 3 Results and Discussion

316 3.1. Macro-mechanical behaviour

317 Samples were hardened for 1 h, 24 h or 28 d and next irradiated at a dose rate of 8.85 kGy/h using a ^{60}Co
 318 source for 22.5 hours. Directly afterwards, uniaxial compressive strength tests on the irradiated and
 319 reference samples were performed. The results are visualised in Figure 5. The compressive strength of the
 320 IP.1.IR samples was higher by a factor 2.2 than the corresponding reference samples. For the IP.24.IR
 321 samples, an increase by a factor 1.81 was registered. For the samples with $t_{\text{prior}} = 28$ days no significant
 322 difference could be observed. Radiation-induced strengthening was already reported by Lambertin et al.
 323 (2013) for geopolymers [31] and by Mast et al. (2019) for iron-rich IPs irradiated at low dose rate [35].
 324 This effect was assigned to a change in pore size distribution or to the growth of carbonates in cracks and
 325 pores [38], [52].



326
 327 **Figure 5:** Compressive strength of irradiated samples compared to the reference with (i) $t_{\text{prior}} = 1$ h, (ii) $t_{\text{prior}} = 24$ h
 328 and (iii) $t_{\text{prior}} = 28$ d – with one standard error of mean.

329 3.2. Micro-mechanical behaviour: nanoindentation¹

330 Micromechanical properties were evaluated using nanoindentation. The samples were tested 14 days after
 331 irradiation. To characterise the fully hardened reference material, the values of IP.28 were used. The results
 332 are summarised in Table 5 and Table 6. The hardness of the unreacted particles was found to be (5.80 ± 0.07) GPa. For the binder phase a value of (1.08 ± 0.07) GPa was found. This is in accordance with the
 333 hardness of the different phases in an IP, reported by Puertas et al. (2011) [53], Lee et al. (2016) [54]
 334 and Nedeljkovic et al. (2018) [56]. In these studies, a hardness in the range of 5 – 10 GPa was reported
 335 for unreacted slag particles and 0.5 – 2 GPa for the IP binder.
 336

337 An indentation modulus of (70 ± 1) GPa was found for the unreacted particles whereas for the binder phase
 338 a value of (25 ± 1) GPa was found. This value is comparable to that of a CSH paste as reported in Lee et
 339 al. (2018) [57]. Both values are also in agreement with the values reported by Nedeljkovic et al. (2018)
 340 [56]. They identified three intervals: $E_m < 4$ GPa for pores, $21 < E_m < 45$ GPa for C-(N-)A-S-H gel and E_m
 341 > 46 GPa for unreacted fly ash and GBFS particles. These intervals are consistent with the results from

¹ In this section, the data is reported as the arithmetic mean \pm one standard error of the mean.

other studies [53], [58], [59]. Lee et al. (2016) [54] reported an indentation modulus range of 4.44-16.78 GPa for pure N-A-S-H phase in fly ash based inorganic polymers and 47.61-70.47 GPa for the non-activated slag particles. These values are of the same order of magnitude as found in this study.

Creep characteristics measured by nanoindentation are reported by Lee et al. (2018) [56]. For the non-activated slag particles, a range in creep modulus (C) of 519 to 1488 GPa was found. For the N-A-S-H gel a creep modulus varying from 41 to 106 GPa was reported. Creep properties in the same order of magnitude were measured for the PS-IPs in this study. For the unreacted particles, a creep modulus of $(1.4 \pm 0.1) \cdot 10^3$ GPa was found. For the binder phase a lower creep modulus of $(1.9 \pm 0.2) \cdot 10^2$ GPa, and thus higher rate of creep was found.

In the following paragraphs, the effect of gamma irradiation will be discussed in more detail. The unreacted particles and the binder phase are discussed separately.

3.2.1. Unreacted particles

The results for the indentation points in unreacted particles are summarised in Table 5. No significant difference could be observed for the hardness between the irradiated and non-irradiated samples. This was in accordance to the assumption that unreacted particles are not affected by irradiation. Average values varying from 5.6 to 6.4 GPa were measured depending on the curing conditions.

For the IP.1, a decrease by a factor of 0.87 was found for the elastic indentation modulus of the irradiated samples. The reference value for non-irradiated samples was (84 ± 2) GPa, while the value for the irradiated sample was (73 ± 2) GPa. For the IP.24 samples an increase by a factor of 1.21 was observed from (57 ± 1) GPa for the non-irradiated samples to (69 ± 1) GPa for the irradiated samples. There seems to be no consistency about the effect of gamma irradiation on the indentation modulus of unreacted slag particles. It should be mentioned that possibly also the underlying binder layers influence the results of the unreacted particles due to the large difference in hardness. No significant difference of the indentation modulus was observed for the 28 days cured samples prior to irradiation.

A higher creep modulus and thus smaller C_{IT} value was found for the IP.1.IR samples compared to the IP.1.REF samples. Relative change in displacement during the creep stage was $(5.1 \pm 0.2)\%$ for the non-irradiated samples and $(2.9 \pm 0.1)\%$ for the irradiated samples, resulting in an increase in creep modulus from $(1.01 \pm 0.05) \cdot 10^3$ GPa to $(3.0 \pm 0.2) \cdot 10^3$ GPa. For the IP.24 samples, the creep modulus increased by a factor of 1.47 from $(1.7 \pm 0.2) \cdot 10^3$ GPa to $(2.5 \pm 0.3) \cdot 10^3$ GPa.

For the 28 days cured samples no significant difference was observed for any of the parameters under consideration. It is observed that unreacted particles in 1 h cured samples are more sensitive to gamma irradiation than longer cured samples. This result is, however, unexpected since it was suggested that slag particles are insensitive to gamma irradiation.

Table 5. Overview of nanoindentation results related to the unreacted slag particles of the irradiated and non-irradiated IPs with Hardness, Indentation modulus, Creep parameter and normalised indentation creep parameter. Parameters for which a significant difference (at 0.05 level) between the irradiated and non-irradiated samples is observed, are marked with a box. It is discouraged to compare sample values to others than their reference sample, since curing conditions can deviate. Sample ID's can be found in Table 3 - one standard error of mean is reported.

	H (GPa)	E_m (GPa)	C (GPa)	C_{IT} (%)
IP.1.REF	6.38 ± 0.07	84 ± 2	$(1.01 \pm 0.05) \cdot 10^3$	5.1 ± 0.2
IP.1.IR	6.2 ± 0.2	73 ± 2	$(3.0 \pm 0.2) \cdot 10^3$	2.9 ± 0.1
IP.24.REF	5.6 ± 0.1	57 ± 1	$(1.7 \pm 0.2) \cdot 10^3$	3.9 ± 0.3
IP.24.IR	5.96 ± 0.07	69 ± 1	$(2.5 \pm 0.3) \cdot 10^3$	2.6 ± 0.4
IP.28.REF	5.80 ± 0.05	70 ± 1	$(1.4 \pm 0.1) \cdot 10^3$	3.8 ± 0.1
IP.28.IR	5.6 ± 0.1	70 ± 2	$(1.1 \pm 0.2) \cdot 10^3$	5.0 ± 0.7

3.2.2. Binder Phase

The nanoindentation results the binder are summarized in Table 6. For IP.1, changes seem to occur as a result of gamma irradiation. The hardness decreased by a factor of 0.73 from (1.20 ± 0.07) GPa to (0.87 ± 0.08) GPa. This might correlate with the increased macroscopic compressive strength [60]. For IP.24, also a significant difference was observed for the hardness. The irradiated samples had a hardness of the binder 1.29 times higher than the non-irradiated samples, (1.19 ± 0.08) GPa and (0.92 ± 0.03) GPa respectively. It appears to be no clear trend about the effect of gamma irradiation on the hardness of the binder phase.

For the IP.1 samples, the Young's modulus decreased by a factor of 0.67 from (32 ± 1) GPa to (21.5 ± 0.9) GPa. For the other samples, no significant difference was observed. A lower creep and thus a higher creep modulus was observed for the irradiated IP.1 samples. The relative change in displacement during the creep stage was $(8.2 \pm 0.6)\%$ for the non-irradiated samples and $(5.9 \pm 0.4)\%$ for the irradiated samples, a decrease by a factor of 0.72. From these results we conclude that the IP binder phase in 1 hour samples are more sensitive to gamma irradiation than older samples.

For the 28 days cured samples no significant difference was observed for any of the parameters under consideration. The hardness was (1.02 ± 0.04) GPa for the non-irradiated samples and (1.07 ± 0.06) GPa for the irradiated samples. Fully hardened cement paste properties of irradiated (257 kGy) an non-irradiated mortar specimens were determined by Hilloulin et al. (2018) [27]. They reported a hardness of (0.41 ± 0.06) GPa and (0.43 ± 0.06) GPa for the reference and the irradiated samples respectively. This indicates that the IP binder in this study is harder than cement paste. The indentation modulus of the 28 days cured IP samples was (25 ± 1) GPa and (23.5 ± 0.9) GPa for the reference and irradiated samples respectively, which is in the same order of magnitude of the indentation modulus obtained for the cement paste: (20 ± 2) GPa in the study of Hilloulin et al. (2018) [27]. For the latter, no significant change after irradiation was observed. IP.28 showed a small decrease in creep modulus from $(1.9 \pm 0.2) \cdot 10^2$ GPa to $(1.5 \pm 0.1) \cdot 10^2$ GPa as a result of irradiation corresponding to an increase of C_{IT} from $(7.1 \pm 0.5)\%$ to $(7.3 \pm 0.4)\%$. Although the creep modulus decreased by a factor of 0.79, it is not considered significant according to the two-sided Student's t-test. Hilloulin et al. (2018) [27] found an increase by 1.17 in creep modulus from $(1.5 \pm 0.2) \cdot 10^2$ GPa to $(1.8 \pm 0.3) \cdot 10^2$ GPa as results of irradiation. It corresponds to a decrease in relative change in displacement from $(5.9 \pm 0.6)\%$ to $(5.3 \pm 0.6)\%$ [27]. Comparing the results of the fully hardened IPs of this study and the mortar samples of Hilloulin et al. (2018) [27] and Robira et al. (2018) [60] is difficult since different experimental set-up was used. The data however suggest that the binding phase of IP is harder and has a slightly higher indentation modulus compared to cement paste. On the other hand, creep is higher for the IP-binder compared to the cement paste. For the IP binder phase it was also found that creep decreases after irradiation, which was also the case for the cement-based mortar samples.

Table 6. Overview of nanoindentation results related to the binder of the irradiated and non-irradiated IPs with a Hardness, Indentation modulus, Creep parameter and normalised indentation creep parameter. Parameters for which a significant difference (at 0.05 level) between the irradiated and non-irradiated samples is observed, are marked with a box. It is discouraged to compare sample values to others than their reference sample, since curing conditions can deviate. Sample ID's can be found in Table 3 - one standard error of mean is reported.

	H (GPa)	E_m (GPa)	C (GPa)	C_{IT} (%)
IP.1.REF	1.20 ± 0.07	32 ± 1	$(1.5 \pm 0.2) \cdot 10^2$	8.2 ± 0.6
IP.1.IR	0.87 ± 0.08	21.5 ± 0.9	$(1.6 \pm 0.3) \cdot 10^2$	5.9 ± 0.4
IP.24.REF	0.92 ± 0.03	22.0 ± 0.7	$(1.8 \pm 0.2) \cdot 10^2$	5.8 ± 0.4
IP.24.IR	1.19 ± 0.08	24 ± 1	$(2.6 \pm 0.4) \cdot 10^2$	6.0 ± 0.6
IP.28.REF	1.02 ± 0.04	25 ± 1	$(1.9 \pm 0.2) \cdot 10^2$	7.1 ± 0.5
IP.28.IR	1.07 ± 0.06	23.5 ± 0.9	$(1.5 \pm 0.1) \cdot 10^2$	7.3 ± 0.4

It can be observed that both the binder phase and the unreacted particles in the 1h cured samples were more sensitive to gamma irradiation than the longer cured samples. Moreover, nanoindentation results show that the binder properties were more affected by gamma irradiation than the unreacted particles. This is related to the higher water content of the binder phase. Water radiolysis leads to reactive species which can affect the properties of the phase. Loss of water as a result of radiolysis and evaporation moreover leads to drying shrinkage of the binder phase. This was not the case for the unreacted particles. This difference in irradiation response causes tensile stress in the hardened inorganic polymer and, eventually, microcracking [61].

Both the unreacted particles and the binder showed an inverse effect of the irradiation on the Young's modulus of the IP.1 compared to the IP.24. In case of IP.1, a decrease due to irradiation was observed while for IP.24 an increase was measured. The same trend was observed for the hardness as for the Young's modulus. It is therefore concluded that the mechanism behind the effect of irradiation are different for non-hardened samples compared to hardened samples. Moreover, fully hardened IP samples (IP.28) seem to withstand irradiations up to 200 kGy without any significant changes in micromechanical properties as such hardness, Young's modulus and creep. It can also be concluded that creep for non-fully hardened samples (IP.1 & IP.24) is lower for irradiated samples compared to non-irradiated samples. A significant increase of 39% in the binder creep modulus for the non-hardened samples (IP.1) could be found.

3.3. Other properties

3.3.1. Mercury Intrusion Porosimetry

The porosity and pore size distribution (PSD) of irradiated and non-irradiated samples were determined using MIP analysis. As shown in Figure 6, for the three curing conditions, the main porosity is related to pores in the 100 - 2000 nm region and pores < 10 nm. The porosity for the IP.1 samples is significantly reduced in the 100 - 2000 nm region as result of irradiation with a shift to the smaller pore sizes. For pores smaller than 10 nm a small shift to the larger pore size diameters was detected. In general, a net lower porosity (- 2.7%) was measured for the irradiated samples compared to the reference samples (Table 7). For the IP.24 samples no significant change could be observed in the PSD apart from the very small shift to the larger pore diameters at 1000 nm, resulting in an increased net total porosity with + 3.0%. For IP.28 no significant change in total porosity was observed. In the PSD plot, however, a shift to the larger pore diameters at 4 - 5 nm was detected and a small shift to the lower pore diameters at 200 - 300 nm was detected. No consensus can be found about the effect of gamma irradiation on the porosity of the tested IPs. For IP.1 samples a shift in PSD to the smaller pore sizes with a decrease in total porosity was reported. For IP.24 and IP.28, no significant but a small increase in porosity was observed. Due to gamma heating and gamma radiolysis, water is eliminated from the geopolymer structure leading to an increased porosity for solidified matrices. For IP.1 samples, on the other hand, which were still viscous at the start of the irradiation, the matrix can shrink plastically without inducing microcracks. It can be concluded that mainly significant changes in the PSD only occur when irradiating non-hardened samples.

Table 7. Porosity of non-irradiated and irradiated samples measured with MIP. The estimated error parameters is $\pm 0.7\%$

	IP.1	IP.24	IP.28
Reference samples	17.0%	14.7%	10.9%
Irradiated samples	15.7%	17.7%	11.6%

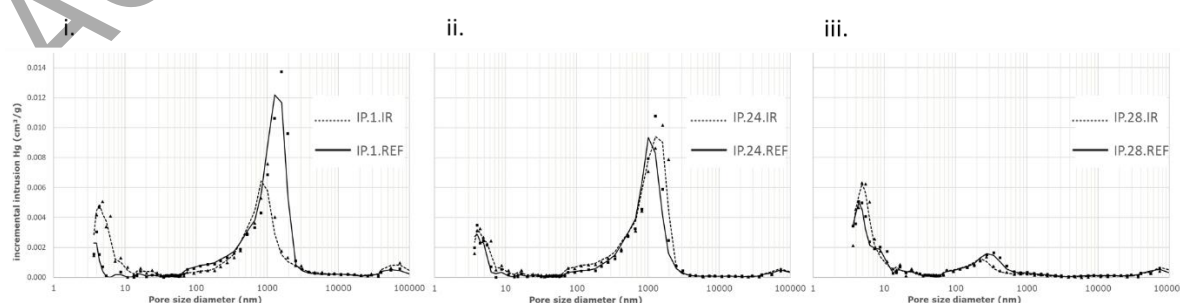
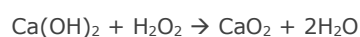


Figure 6: Pore size distribution of the irradiated samples compared to the reference samples with (i) $t_{\text{prior}} = 1$ h, (ii) $t_{\text{prior}} = 24$ h and (iii) $t_{\text{prior}} = 28$ d.

3.3.2. ATR-FTIR

Infrared spectra of the different samples do not indicate a difference as a result of irradiation. Only a small decrease in water content for the irradiated samples can be observed. As an example, the infrared spectra of IP.24 are presented in Figure 7. The IR peak from 3000 – 3500 cm⁻¹ and from 1650 – 1655 cm⁻¹ are correlated to the water content of the samples. Around 1400 cm⁻¹ the peak for Si-O-Si bond stretching can be found. At 950 cm⁻¹ – 1250 cm⁻¹ the Si-O-T (with T = Al or Si) asymmetric and symmetric stretching and vibration is found. At 680 cm⁻¹ the value for Si-O stretching vibration is located and at 440 cm⁻¹ T-O bending vibration response is detected. No difference for carbonates (± 1400 cm⁻¹) as a result of irradiation was observed. This differs from a previous study [35] in which an extra peak at 1404 cm⁻¹ was observed related to CaCO₃. Radiation-induced carbonation at high dose rate irradiation can thus not be confirmed in the current study. Radiation-induced carbonation was earlier observed by Maruyama et al. (2018) when irradiating fully hydrated OPC mortars up to 5 x 10⁴ kGy at ± 7 kGy/h [52]. Carbonates were formed as the result of the reaction of Ca(OH)₂ (forming after cement hydration) with H₂O₂ (formed from radiolysis) towards insoluble calcium peroxide, CaO₂.8H₂O [62]. The peroxide is very slightly soluble and easily loses its water of crystallization [52]. Dehydrated peroxide reacts with water to form portlandite Ca(OH)₂ which in turn can react with CO₂ to form CaCO₃ [13], [52]. Notice that the presence of Ca(OH)₂ results in the consumption of the radiolytic H₂O₂ (equation 9) [52], [62].



Equation 9

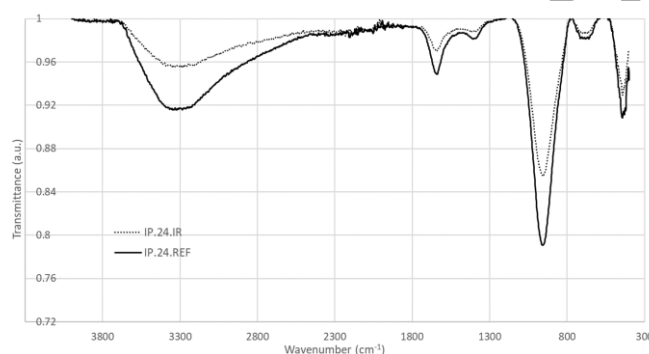


Figure 7: ATR-FTIR spectra of the irradiated samples compared to the reference samples for IP.24.

3.3.3. Thermogravimetric analysis

The first mass loss from 20 °C to 250 °C in the TGA curves is attributed to the dehydration of free evaporable water and interstitial water. The TGA results (Figure 8) indicate a lower water content for the irradiated samples which is in agreement with the ATR-FTIR results. This is related to water radiolysis during irradiation and due to the accelerated evaporation of water as a result of gamma heating. During irradiation the temperature evolution in a cubic (20 x 20 x 20) mm³ sample was monitored. A thermocouple was placed in the centre of a sample accessible through a 5 mm diameter drilled hole. A temperature increase from 25.4 °C to 34.2 °C was registered. TGA results indicate that higher t_{prior} lead to less water loss as a result of irradiation.

The weight loss from 250 °C to 700 °C can be attributed to bound water present in the hydrates [5], [63]. In this region no difference could be observed. In the region from 570 °C to 620 °C however, a small difference was observed. This was clearly visible for the IP.24 and IP.28 samples and can be related to the decomposition of (calcium) carbonates [64], [65]. According to Thiery et al. (2007) [66], who investigated carbonation in cementitious materials, this temperature interval can be associated to the crystalline and metastable polymorph of CaCO₃: vaterite. Similar effects are observed in a previous study [35]. From the TGA curves it can be concluded that more carbonates decompose for the reference samples than for the irradiated samples. However, since samples were grinded before TGA analysis, local carbonation could also occur during sample preparation.

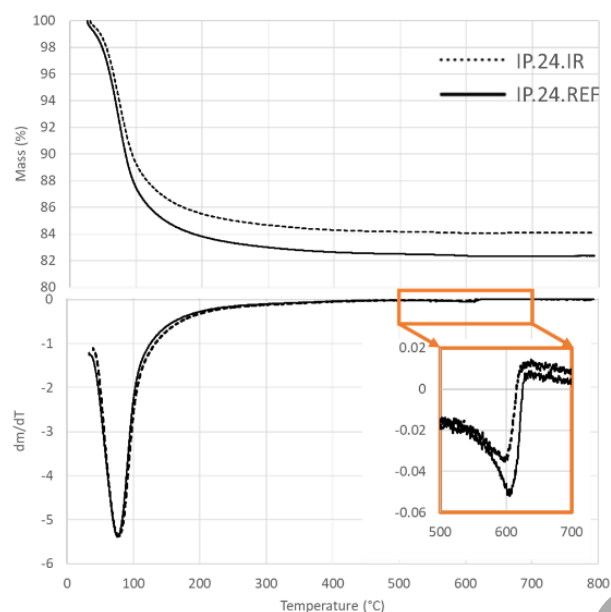


Figure 8: TGA curves and dm/dT curves of the irradiated and non-irradiated IP.24 samples from 25 °C to 800 °C with a zoomed view of the dm/dT curves from 500 °C to 700 °C.

3.3.4. ^{57}Fe Mössbauer spectroscopy

Mössbauer spectroscopy was used to determine the redox ratio of ferric (Fe^{3+}) and ferrous (Fe^{2+}) iron in the irradiated and non-irradiated IP samples. All spectra are fitted with a model using three quadrupole split components (C1, C2 and C3) as visualised in Figure 9 for the case of the IP.24.REF sample spectrum. The different raw spectra of all samples are compared in Figure 10. The relative absorption areas (RAA) are calculated for each component and reported in Table 8. Based on these RAAs, the $\text{Fe}^{3+}/\Sigma\text{Fe}$ ratio and $\text{Fe}^{2+}/\Sigma\text{Fe}$ ratio can be calculated. According to Mysen (2006) [67], the isomeric shift (IS) most probable values for Fe^{3+} at RT are found between 0.23 and 0.41 mm/s within a range of distributions from 0.12 to 0.40 mm/s and the quadrupole splitting (QS) values between 1.06 and 1.61 mm/s within a range of distributions from 0.10 to 0.74 mm/s. The corresponding IS and QS values for Fe^{2+} at RT are reported there to lie from 0.91 to 1.14 mm/s within a range of distributions from 0.06 to 0.45 mm/s and 1.64 to 2.08 mm/s within a range of distributions from 0.11 to 0.60 mm/s, respectively. Both parameters are also reported there with a tendency to decrease with increasing $\text{Fe}^{3+}/\Sigma\text{Fe}$ ratio. Taking into account these characteristics, from the IS and QS values reported in Table 8, components C1 and C2 are characterized as Fe^{2+} and component C3 as Fe^{3+} [68].

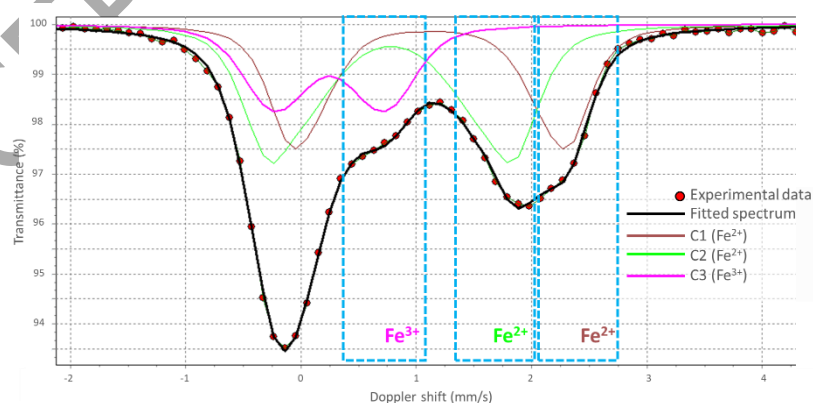


Figure 9: ^{57}Fe Mössbauer experimental spectrum of IP.24.REF (points) with the fitted components in different colours. The dashed rectangles indicate the regions where the contributions from the higher velocity parts of the Fe^{3+} and Fe^{2+} quadrupole split doublets appear.

528 A RAA(Fe^{3+}) of 20% was found for IP.1.REF, while for IP.1.IR a RAA(Fe^{3+}) was found of 39%. This indicates
529 clearly that gamma irradiation stimulates the oxidation of iron in the IP matrix. Also for IP.24 an increase
530 in RAA(Fe^{3+}) was observed. The relative amount of Fe^{3+} increased from 24% to 38%. However, for IP.28
531 no increase in Fe^{3+} content is observed as a result of irradiation. Both the irradiated and non-irradiated
532 samples had a RAA(Fe^{3+}) of 43%. It can thus be concluded that non-hardened samples ($t_{\text{prior}} = 1$ h) are
533 more sensitive to iron oxidation as a result of gamma irradiation than hardened samples. Radiation-induced
534 oxidation of Fe^{2+} is associated to the formation of iron oxyhydroxide. We believe the oxidation in IPs is
535 caused by radiolytically produced $\bullet\text{OH}$ radicals as explained in section 3.3.5. The extent of the phenomenon
536 can be explained by the evolution of the water and of the dissolved Fe^{2+} content. Since both decrease in
537 time, a longer curing time prior to irradiation leads to less radiation-induced iron oxidation. Water in the
538 samples decreases over time as a result of natural evaporation. The Fe^{2+} content decreases in function of
539 time as a result of the natural oxidation of iron as a result of the polymerisation reactions, which reduces
540 the amount of Fe^{2+} iron, susceptible to oxidation, in the sample with time [10]. This is indicated by the
541 increase of the $\text{Fe}^{3+}/\Sigma\text{Fe}$ ratio for the reference samples with increasing $t_{\text{prior}} = [1 \text{ h}, 24 \text{ h}, 28 \text{ d}]$: 20%, 24% and
542 43%. Future experiments will give better insight in the process taking place.

543 **Table 8.** Hyperfine parameters values resulting from the components used to fit the ^{57}Fe Mössbauer spectra. IS stands
544 for isomer shift given relative to $\alpha\text{-Fe}$ at RT, QS is the central value of the quadrupole splitting and the RAA is the
545 relative absorption area of each component. The estimated errors on the parameters are ± 0.02 mm/s for IS and QS,
546 and $\pm 5\%$ for the absorption area.

Component		IS (mm/s)	QS (mm/s)	RAA (%)	Effect of irradiation on RAA
IP.1.REF	C1 - (Fe^{2+})	1.22	2.32	38	
	C2 - (Fe^{2+})	0.88	1.99	42	
	C3 - (Fe^{3+})	0.35	0.92	20	
IP.1.IR	C1 - (Fe^{2+})	1.19	2.14	20	↓
	C2 - (Fe^{2+})	0.95	1.84	41	≈
	C3 - (Fe^{3+})	0.33	0.95	39	↑
IP.24.REF	C1 - (Fe^{2+})	1.22	2.30	32	
	C2 - (Fe^{2+})	0.89	1.96	44	
	C3 - (Fe^{3+})	0.35	0.92	24	
IP.24.IR	C1 - (Fe^{2+})	1.17	2.13	17	↓
	C2 - (Fe^{2+})	0.97	1.79	45	≈
	C3 - (Fe^{3+})	0.33	0.89	38	↑
IP.28.REF	C1 - (Fe^{2+})	1.19	2.16	9	
	C2 - (Fe^{2+})	0.98	1.88	48	
	C3 - (Fe^{3+})	0.37	0.80	43	
IP.28.IR	C1 - (Fe^{2+})	1.21	2.21	10	≈
	C2 - (Fe^{2+})	0.99	1.85	47	≈
	C3 - (Fe^{3+})	0.36	0.85	43	≈

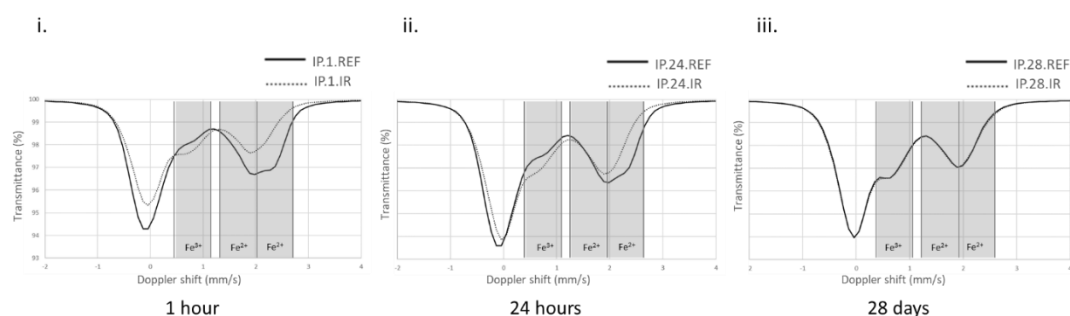


Figure 10: Comparison of the raw ^{57}Fe Mössbauer spectra of the irradiated and non-irradiated samples with (i) $t_{\text{prior}} = 1$ h, (ii) $t_{\text{prior}} = 24$ h and (iii) $t_{\text{prior}} = 28$ d. The shaded areas indicate the regions of the higher velocity parts of the Fe^{3+} and the Fe^{2+} doublets used to fit the spectra.

3.3.5. Radiation-induced oxidation of iron

Radiation-induced oxidation of Fe^{2+} has already been widely studied for applications other than inorganic polymers. Radiation-induced oxidation of iron is currently used as technique to control the formation of iron oxide nanoparticles for use in cancer treatment, environmental clean-up, catalysis and gas sensors [69]–[72]. Gamma-irradiation synthesis is used for the reduction or oxidation of metal ions, followed by metal clustering in nuclei growth. This technique makes use of the strong reducing ($\bullet\text{e}_{\text{aq}}^-$, $\bullet\text{H}$) and oxidising species ($\bullet\text{OH}$, H_2O_2) formed as a result of water radiolysis. When the irradiation is terminated, the reactive species recombine to reform into water [70].

According to Wren et al. (2010) [73], in alkaline conditions ($\text{pH} > 8.5$) the main radiolysis products are molecular H_2 , O_2 and H_2O_2 . Upon irradiation their concentration accumulates very quickly, followed by a slower increase, taking a few hours to reach the steady-state level. The redox reactions taking place are dependent on the pH of the environment. At $\text{pH} < 9.7$, $\bullet\text{e}_{\text{aq}}^-$ is removed by reaction with H^+ (equation 10). At higher pH's however, which is the case for most IPs, this reaction becomes too slow and the removal path of $\bullet\text{e}_{\text{aq}}^-$ shifts to a reaction with the secondary radiolysis product, O_2 , originating from the disproportionation reaction of $\bullet\text{O}_2^-$ ($/\text{HO}_2\bullet$). A reaction loop is established in which O_2 acts as a catalyst for $\bullet\text{e}_{\text{aq}}^-$ and $\bullet\text{OH}$ removal (equation 11, 12). The effect is an increase in concentrations of H_2 and H_2O_2 , since these products normally decompose as a result of the reaction with $\bullet\text{e}_{\text{aq}}^-$ or $\bullet\text{OH}$ [73]. H_2O_2 is a strong oxidant and can cause iron oxidation in for example the inorganic polymer samples. We note that according to equation 9, the calcium content in a sample might suppress this effect of iron oxidation as a result of the consumption of H_2O_2 by $\text{Ca}(\text{OH})_2$ to produce calcium peroxide.



Wren et al. (2010) [73] reported the formation of iron oxyhydroxide ($\text{FeO}(\text{OH})$) nanoparticles from dissolved Fe^{2+} . In this process, dissolved Fe^{2+} was oxidised to Fe^{3+} by radiolytically produced $\bullet\text{OH}$ radicals and H_2O_2 , followed by the hydrolysis of Fe^{3+} with the precipitation of $\text{Fe}(\text{OH})_3$. Nevertheless, no precipitation was observed by Wren et al. (2010) [73] although the solubility limits were exceeded. Instead, a colloid formation of Fe^{3+} oxy-hydroxide was observed [73]. The formation of islands of Fe_2O_3 on the surfaces of FeO and Fe_3O_4 as a result of irradiation was also reported by Sarah et al. (2019) [71]. Sutherland et al. (2016) [70] reported the formation of magnetite particles as a result of the gamma irradiation of FeSO_4 solutions. In silicate free IP systems, colloidal $\text{FeO}(\text{OH})$ as observed by Wren et al. (2010) might be formed [73]. In this study, however, the aqueous silica from the activation solution can inhibit the Fe^{3+} hydrolysis via the formation of stable ferric silicate complexes [74], [75].

Oxidising $\bullet\text{OH}$ radicals are produced in the Fenton's reaction. Ferrous iron acts as a catalyst in this reaction scheme leading to the disproportionation of hydrogen peroxide (equation 14) with the production of very oxidising $\bullet\text{OH}$ radicals [76]. These radicals can even attack $\text{Fe}(\text{III})$ to form $\text{Fe}(\text{IV})$ species [76]. Bouniol (2010) [77] found that at high pH (>13) ferryl-based complexes ($\text{Fe}(\text{OH})_4^-$) become the main oxidising species being formed. It is concluded that radiolysis leads to the coexistence of $\text{Fe}(\text{II})$, $\text{Fe}(\text{III})$ and $\text{Fe}(\text{IV})$ [77], [78]. Fe^{2+} ions are more easily oxidised by $\bullet\text{OH}$ radicals than Fe^{3+} ions are reduced by $\bullet\text{e}_{\text{aq}}^-$ and $\bullet\text{O}_2^-$, thus giving a possible explanation for the iron oxidation in the IP samples. [73].

592 Radiolytic oxidation: $\text{Fe}^{2+} + \bullet\text{OH} \rightarrow \text{Fe}^{3+} + \text{OH}^-$ Equation 13

593 $2\text{Fe}^{2+} + \text{H}_2\text{O}_2 \rightarrow 2\text{Fe}^{3+} + 2\text{OH}^-$

594 Fenton Reaction: $\text{Fe}^{2+} + \text{H}_2\text{O}_2 \rightarrow \text{Fe}^{3+} + \bullet\text{OH} + \text{OH}^-$

595 $\text{Fe}^{3+} + \text{H}_2\text{O}_2 \rightarrow \text{Fe}^{2+} + \bullet\text{OOH} + \text{H}^+$ Equation 14

596 Hydrolysis of ferric ions: $\text{Fe}^{3+} + 3\text{OH}^- \leftrightarrow \text{Fe}(\text{OH})^{2+} + 2\text{OH}^- \leftrightarrow \text{Fe}(\text{OH})_2^+ + \text{OH}^- \leftrightarrow \text{Fe}(\text{OH})_3 \leftrightarrow \text{FeO}(\text{OH}) + \text{H}_2\text{O}$

597
598 Equation 15

599 Since inorganic polymers are known to be highly alkaline materials (pH > 11) the reaction mechanisms as
600 in equation 13-15 can lead to an increased $\text{Fe}^{3+}/\text{Fe}^{2+}$ ratio in the IP gel and pore solution. Especially in the
601 initial reaction stage of the IP, when unbound Fe^{2+} can still be found, the effect of radiation-induced iron
602 oxidation is expected to have the highest impact. Since in function of time more Fe-atoms will be bound in
603 the IP structure, oxidation of iron becomes more difficult. As the main oxidation of $\text{CaO-FeO}_x\text{-SiO}_2$ in IP
604 samples happens during the first 24 h, irradiation during this reaction stage can have a large impact on
605 the final sample [10]. Since Fe^{2+} and Fe^{3+} are incorporated in the IP 3D structure in different ways, a
606 change in $\text{Fe}^{3+}/\text{Fe}^{2+}$ ratio leads to the formation in different phases in the material and can influence the
607 final macroscopic strength. It is suggested that tetrahedral Fe^{3+} takes place in the silicate framework [10],
608 [79] while Fe^{2+} takes place in a trioctahedral layer [10]. The contribution of ferryl ions to the IP
609 microstructure has not been investigated. The valence however suggests ferryl to contribute to the silicate
610 framework.

611 The effect of irradiation on unsolidified samples is of importance when considering these materials as
612 conditioning matrix for nuclear waste, since these materials are subjected to gamma irradiation from time
613 zero. A side note should be made that in the presence of iron also causes more H_2 to be produced. Radicals
614 such as $\bullet\text{O}^-$ react faster with iron species than they do with H_2 thus increasing the survival rate of H_2 [77],
615 [80]. Moreover, $\bullet\text{e}_{\text{aq}}^-$ and $\bullet\text{O}^-$ are potentially trapped in the $\text{Fe(II)} \leftrightarrow \text{Fe(III)}$ oxidation-reduction equilibrium
616 thus reducing their reaction potential with H_2 [80].

617 4 Conclusions

618 Iron-rich $\text{CaO-FeO}_x\text{-SiO}_2$ slag-based inorganic polymer samples were hardened for 1 h, 24 h or 28 d and
619 next irradiated for 22.5 hours at a dose rate of 8.85 kGy/h using a ^{60}Co source. Several properties of the
620 samples were evaluated after irradiation and compared to the non-irradiated materials. An overview of the
621 effects related to the gamma irradiation is given in Table 9. It is indicated that samples of only 1 hour old
622 prior to irradiation (IP.1) are affected more by gamma irradiation than hardened samples (IP.24 & IP.28).
623 28 days cured samples are found to be resistant to the irradiation for the dose(rate) tested without any
624 significant changes for the executed tests. From the results of IP.1 and IP.24 it is clear that the irradiation
625 response depends highly on the materials condition at the start of the irradiation. For the change in
626 hardness and the change in pore size distribution, an opposite effect could be observed when comparing
627 IP.1 tot IP.24. Since IP.1 samples are still viscous at the start of the irradiation, the matrix can more easily
628 shrink, thus leading to a decrease in porosity. Moreover, it is indicated by nanoindentation that the binder
629 is more sensitive to gamma irradiation than the unreacted particles, which is related to the higher water
630 content of the binder phase.

631 For non-fully hardened samples (IP.1 and IP.24), it can be concluded that gamma irradiation increases the
632 macromechanical compressive strength. This effect can be related to the accelerated dehydration at the
633 early age of the sample, causing densification of the samples. Strengthening of the samples however can
634 also be related to the increase in Fe^{3+} content as a result of gamma irradiation, since Fe^{3+} can take place
635 in the silicate network. Radiation-induced iron oxidation occurs as Fe^{2+} from the slag dissolution is oxidised
636 by radiolytically produced $\bullet\text{OH}$ radicals and H_2O_2 . Especially in the initial reaction stage of the IP, when
637 unbound Fe^{2+} can still be found, the effect of radiation-induced iron oxidation is expected to have the
638 highest impact. In function of time, radiation-induced oxidation becomes more difficult as the samples
639 dehydrate and since more Fe-atoms will be bound in the IP structure. Changes in the $\text{Fe}^{3+}/\text{Fe}^{2+}$ ratio can
640 lead to the formation of different phases in the material which can influence the macroscopic strength.

641 For the IP.1 samples multiple effects were observed: an increase of the compressive strength by a factor
642 of 2.20, a lower Young's-modulus, lower creep in time, a decrease in porosity by a factor of 0.92, and an
643 increase of the $\text{Fe}^{3+}/\Sigma\text{Fe}$ ratio by a factor of 1.95. A significant decrease by a factor of 0.67 for the binder
644 indentation modulus and a significant decrease by a factor of 0.72 for the binder creep was found.

645
646
647

Table 9. Summary of the irradiation effects observed for the samples with $t_{\text{prior}} = 1 \text{ h}$, 24 h and 28 d . $\uparrow\uparrow$ indicates a strong increase as a result of irradiation, \uparrow indicates an increase as result of irradiation, \approx indicates that there is no significant change as a result of irradiation and \downarrow indicates a decrease as a result of irradiation.

	IP.1	IP.24	IP.28
Macromechanical compressive strength	$\uparrow\uparrow$	\uparrow	\approx
Hardness (binder)	\downarrow	\uparrow	\approx
Indentation modulus (binder)	\downarrow	\approx	\approx
Creep (binder)	\downarrow	\downarrow	\approx
Total open porosity	\downarrow	\uparrow	\approx
Free water content	\downarrow	\downarrow	\approx
Carbonates	\approx	\downarrow	\downarrow
$\frac{Fe^{3+}}{\Sigma Fe}$ ratio	$\uparrow\uparrow$	\uparrow	\approx

648

649 **Data availability**

650 The raw/processed data required to reproduce these findings cannot be shared at this time as the data also
651 forms part of an ongoing study.

652 **Acknowledgements**

653 The authors express their appreciation to dr. ing. Krzysztof Kierzek from Wroclaw University of Science and
654 Technology to perform the MIP-analysis. The authors also thank L. Arnout and L. Machiels from KU Leuven
655 from providing the synthetic plasma slag. This study was partially supported by the Special Research Fund
656 (BOF) of Hasselt University, by the ENEN+ project that has received funding from the Euratom research
657 and training Work Programme 2 and by the Research Funding Flanders (FWO). The experimental data used
658 in this research were partially generated through access to the ActUsLab-FMR under the Framework of
659 access to the Joint Research Centre Physical Research Infrastructures of the European Commission (IP4NA
660 project, Research Infrastructure Access Agreement Nr.35433). APD acknowledges the partial support of
661 this work by the project MIS 5002772, implemented under the Action "Reinforcement of the Research and
662 Innovation Infrastructure", funded by the Operational Programme "Competitiveness, Entrepreneurship and
663 Innovation" (NSRF 2014-2020) and co-financed by Greece and the European Union (European Regional
664 Development Fund).

References

- [1] J. Davidovits, "Geopolymer, Green Chemistry and Sustainable Development Solutions," in *Proceedings of the World Congress Geopolymer 2005*, 2005, p. 236.
- [2] J. L. Provis and J. S. J. Van Deventer, *Alkali-Activated Materials- State-of-the-Art Report*, RILEM TC 224-AAM, vol. 13. London: Springer, 2014.
- [3] B. Mast, Y. Pontikes, W. Schroevers, B. Vandoren, and S. Schreurs, "The use of alkali activated materials in nuclear industry," in *Comprehensive Nuclear Materials*, 2nd ed., R. Konings, Ed. Elsevier Inc., 2020.
- [4] M. Danthurebandara, S. Van Passel, L. Machiels, and K. Van Acker, "Valorization of thermal treatment residues in Enhanced Landfill Mining: Environmental and economic evaluation," *J. Clean. Prod.*, vol. 99, pp. 275–285, 2015.
- [5] L. Kriskova, L. Machiels, and Y. Pontikes, "Inorganic Polymers from a Plasma Converter Slag : Effect of Activating Solution on Microstructure and Properties," *J. Sustain. Met.*, vol. 1, no. 3, pp. 240–251, 2015.
- [6] L. Machiels, L. Arnout, E. Nagels, S. Arnout, B. Blanpain, and Y. Pontikes, "Properties of inorganic polymer cement from ferric and ferrous vitrified residues of plasma gasification," in *Proceedings of the 4th slag valorisation symposium - Zero Waste*, 2015, pp. 319–324.
- [7] L. Machiels, L. Arnout, P. Yan, P. Tom Jones, B. Blanpain, and Y. Pontikes, "Transforming Enhanced Landfill Mining Derived Gasification / Vitrification Glass into Low-Carbon Inorganic Polymer Binders and Building Products," *J. Sustain. Metall.*, vol. 3, no. 2, pp. 405–415, 2016.
- [8] A. Peys, C. E. White, D. Olds, H. Rahier, B. Blanpain, and Y. Pontikes, "Molecular structure of CaO – FeOx – SiO₂ glassy slags and resultant inorganic polymer binders," *J. Am. Ceram. Soc.*, vol. 101, no. 12, pp. 5846–5857, 2018.
- [9] A. Peys, "Inorganic polymers from CaO-FeO-SiO₂ slags - processing, reaction mechanism and molecular structure," KULeuven, 2018.
- [10] A. Peys, A. P. Douvalis, V. Hallet, H. Rahier, B. Blanpain, and Y. Pontikes, "Inorganic Polymers From CaO-FeOx-SiO₂ Slag: The Start of Oxidation of Fe and the Formation of a Mixed Valence Binder," *Front. Mater.*, vol. 6, no. 212, pp. 1–10, 2019.
- [11] J. Van De Sande, A. Peys, T. Hertel, H. Rahier, and Y. Pontikes, "Upcycling of non-ferrous metallurgy slags: Identifying the most reactive slag for inorganic polymer construction materials," *Resour. Conserv. Recycl.*, vol. 154, 2020.
- [12] T. Croymans-Plaghki, "Valorization of Fe-rich industrial by-products in construction materials: a radiological assessment," UHasselt, 2018.
- [13] G. L. Bykov, A. V. Gordeev, T. K. Yurik, and B. G. Ershov, "Gas formation upon γ -irradiation of cement material," *High Energy Chem.*, vol. 42, no. 3, pp. 211–214, 2008.
- [14] B. Craeye, "Early-Age Thermo-Mechanical Behaviour of Concrete Supercontainers for Radwaste Disposal," 2010.
- [15] W. Wacquier, "Summary of the Safety Report for the surface repository of category A waste in Dessel," 2012.
- [16] E. R. Vance and D. S. Perera, "Development of geopolymers for nuclear waste immobilisation," in *Handbook of Advanced Radioactive Waste Conditioning Technologies*, Woodhead Publishing Limited, 2011, pp. 207–229.
- [17] D. G. Bennett and R. Gens, "Overview of European concepts for high-level waste and spent fuel disposal with special reference waste container corrosion," *J. Nucl. Mater.*, vol. 379, no. 1–3, pp. 1–8, 2008.
- [18] T. M. Rosseel et al., "Radiation Damage In Reactor Cavity Concrete," in *Contribution of Materials Investigations and Operating Experience to LWRs' Safety, Performance and Reliability*, 2014.
- [19] I. Remec, T. M. Rosseel, K. G. Field, and Y. Le Pape, "Characterization of Radiation Fields for Assessing Concrete Degradation in Biological Shields of NPPs Biological Shields," *EPJ Web Conf.*, vol. 153, pp. 1–4, 2017.
- [20] H. K. Hilsdorf, J. Kropp, and H. J. Koch, "The Effects of Nuclear Radiation on the Mechanical Properties of Concrete," *Am. Concr. Inst.*, vol. 55, pp. 223–254, 1978.

- 717 [21] T. Ichikawa and H. Koizumi, "Possibility of Radiation-Induced Degradation of Concrete by Alkali-
718 Silica Reaction of Aggregates," *J. Nucl. Sci. Technol.*, vol. 39, no. 8, pp. 880–884, 2012.
- 719 [22] P. Soo and L. Milian, "The effect of gamma radiation on the strength of Portland cement mortars,"
720 *J. Mater. Sci. Lett.*, vol. 20, no. 14, pp. 1345–1348, 2001.
- 721 [23] F. Vodák, V. Vydra, K. Trtík, and O. Kapičková, "Effect of gamma irradiation on properties of
722 hardened cement paste," *Mater. Struct.*, vol. 44, no. 1, pp. 101–107, 2010.
- 723 [24] T. M. Rosseel *et al.*, "Review of the Current State of Knowledge on the Effects of Radiation on
724 Concrete," *J. Adv. Concr. Technol.*, vol. 14, no. 7, pp. 368–383, 2016.
- 725 [25] O. Kontani, S. Sawada, I. Maruyama, M. Takizawa, and O. Sato, "Evaluation of Irradiation Effects
726 on Concrete Structure: Gamma-Ray Irradiation Tests on Cement Paste," in *Proceedings of the ASME*
727 *2013 Power Conference POWER2013*, 2013.
- 728 [26] A. Łowińska-Kluge and P. Piszora, "Effect of gamma irradiation on cement composites observed with
729 XRD and SEM methods in the range of radiation dose 0-1409 MGy," *Natl. Meet. Synchrotron Radiat.*
730 *Users*, vol. 114, no. 2, pp. 399–411, 2008.
- 731 [27] B. Hilloulin, M. Robira, and A. Loukili, "Coupling statistical indentation and microscopy to evaluate
732 micromechanical properties of materials : Application to viscoelastic behavior of irradiated mortars,"
733 *Cem. Concr. Compos.*, vol. 94, pp. 153–165, 2018.
- 734 [28] F. Chupin, A. Dannoux-papin, Y. N. Ravache, and J.-B. D'Espinose de Lacaillerie, "Water content
735 and porosity effect on hydrogen radiolytic yields of geopolymers," *J. Nucl. Mater.*, vol. 494, pp. 138–
736 146, 2017.
- 737 [29] A. Rooses, P. Steins, A. Dannoux-Papin, D. Lambertin, A. Poulesquen, and F. Frizon, "Encapsulation
738 of Mg-Zr alloy in metakaolin-based geopolymer," *Appl. Clay Sci.*, vol. 73, no. 1, pp. 86–92, 2013.
- 739 [30] W. Li, P. N. Lemougna, K. Wang, Y. He, Z. Tong, and X. Cui, "Effect of vacuum dehydration on gel
740 structure and properties of metakaolin-based geopolymers," *Ceram. Int.*, vol. 43, no. 16, pp.
741 14340–14346, 2017.
- 742 [31] D. Lambertin, C. Boher, A. Dannoux-Papin, K. Galliez, A. Rooses, and F. Frizon, "Influence of gamma
743 ray irradiation on metakaolin based sodium geopolymer," *J. Nucl. Mater.*, vol. 443, no. 1–3, pp.
744 311–315, 2013.
- 745 [32] F. Chupin, "Caractérisation de l'effet des irradiations sur les géopolymères," Université Pierre et
746 Marie Curie, 2015.
- 747 [33] V. Cantarel, M. Arisaka, and I. Yamagishi, "On the hydrogen production of geopolymer wasteforms
748 under irradiation," *J. Am. Ceram. Soc.*, vol. 102, no. 12, pp. 7553–7563, 2019.
- 749 [34] L. Leay, A. Potts, and T. Donocli, "Geopolymers from fly ash and their gamma irradiation," *Mater.*
750 *Lett.*, vol. 227, pp. 240–242, 2018.
- 751 [35] B. Mast *et al.*, "The effect of gamma radiation on the mechanical and microstructural properties of
752 Fe-rich inorganic polymers," *J. Nucl. Mater.*, vol. 521, 2019.
- 753 [36] T. A. Mubasher, L. Leay, M. Hayes, and E. Butcher, "Evaluation of Novel Geopolymer-based Materials
754 for Nuclear Waste Treatment," in *NUWCEM - 3rd International Symposium on Cement-Based*
755 *Materials for Nuclear Wastes*, 2018, pp. 1–5.
- 756 [37] N. Deng *et al.*, "Effects of gamma-ray irradiation on leaching of simulated $^{137}\text{Cs}^+$ radionuclides
757 from geopolymer wasteforms," *J. Nucl. Mater.*, vol. 459, pp. 270–275, 2015.
- 758 [38] I. Maruyama *et al.*, "Impact of gamma-ray irradiation on hardened white Portland cement pastes
759 exposed to atmosphere," *Cem. Concr. Res.*, vol. 108, pp. 59–71, 2018.
- 760 [39] European Committee for standardization, "EN 196-6:2010 - Methods of testing cement - Part 6:
761 Determination of fineness," pp. 1–18, 2010.
- 762 [40] G. Ascensão, G. Beersaerts, M. Marchi, M. Segata, F. Faleschini, and Y. Pontikes, "Shrinkage and
763 mitigation strategies to improve the dimensional stability of $\text{CaO-FeOx-Al}_2\text{O}_3\text{-SiO}_2$ inorganic
764 polymers," *Materials (Basel)*, vol. 12, no. 22, 2019.
- 765 [41] A. F. Fernandez *et al.*, "SCK-CEN gamma irradiation facilities for radiation tolerance assessment,"
766 *IEEE Radiat. Eff. Data Work.*, vol. 2002-Janua, pp. 171–176, 2002.
- 767 [42] A. F. Fernandez, B. Brichard, H. Ooms, and F. Berghmans, "Gamma dosimetry using red 4034

- 768 Harwell dosimeters in mixed gamma-neutron environments," *Eur. Sp. Agency, (Special Publ. ESA*
769 *SP*, vol. 2003-Septe, no. 2, pp. 517–521, 2003.
- 770 [43] A. F. Fernandez, B. Brichard, H. Ooms, and F. Berghmans, "High-vacuum gamma irradiation facilities
771 for synergistic effects testing on optoelectronic components and materials," *IEEE Trans. Nucl. Sci.*,
772 vol. 53, no. 6, pp. 3726–3730, 2006.
- 773 [44] H. Dosimeters, "Harwell Amber 3042 Dosimeters." [Online]. Available: [http://www.harwell-](http://www.harwell-dosimeters.co.uk/harwell-amber-3042/)
774 [dosimeters.co.uk/harwell-amber-3042/](http://www.harwell-dosimeters.co.uk/harwell-amber-3042/).
- 775 [45] Bureau voor Normalisatie, "NBN EN 12390-3 - Testing hardened concrete - Part 3: Compressive
776 strength of test specimens," 2nd ed., 2009.
- 777 [46] M. Miller, C. Bobko, M. Vandamme, and F. Ulm, "Surface roughness criteria for cement paste
778 nanoindentation," vol. 38, no. 4, pp. 467–476, 2008.
- 779 [47] M. Nedeljkovic, B. Šavija, Y. Zuo, M. Lukovic, and G. Ye, "Effect of natural carbonation on the pore
780 structure and elastic modulus of the alkali-activated fly ash and slag pastes," *Constr. Build. Mater.*,
781 vol. 161, pp. 687–704, 2018.
- 782 [48] W. C. Oliver and G. M. Pharr, "An improved technique for determining hardness and elastic modulus
783 using load and displacement sensing indentation experiments," *J. Mater. Res.*, vol. 7, no. 6, pp.
784 1564–1583, 1992.
- 785 [49] M. Vandamme, C. A. Tweedie, G. Constantinides, F. J. Ulm, and K. J. Van Vliet, "Quantifying
786 plasticity-independent creep compliance and relaxation of viscoelastoplastic materials under contact
787 loading," *J. Mater. Res.*, vol. 27, no. 1, pp. 302–312, 2012.
- 788 [50] Q. Zhang, R. Le Roy, M. Vandamme, and B. Zuber, "Long-term creep properties of cementitious
789 materials: Comparing microindentation testing with macroscopic uniaxial compressive testing,"
790 *Cem. Concr. Res.*, vol. 58, pp. 89–98, 2014.
- 791 [51] P. Douvalis, A. Polymeros, and T. Bakas, "IMSG09: A ^{57}Fe - ^{119}Sn Mössbauer spectra computer
792 fitting program with novel interactive user interface," *J. Phys. Conf. Ser.*, vol. 217, no. 1, 2010.
- 793 [52] P. Bouniol and A. Aspart, "Disappearance of oxygen in concrete under irradiation: The role of
794 peroxides in radiolysis," *Cem. Concr. Res.*, vol. 28, no. 11, pp. 1669–1681, 1998.
- 795 [53] F. Puertas, M. Palacios, H. Manzano, J. S. Dolado, A. Rico, and J. Rodríguez, "A model for the C-A-
796 S-H gel formed in alkali-activated slag cements," *J. Eur. Ceram. Soc.*, vol. 31, no. 12, pp. 2043–
797 2056, 2011.
- 798 [54] H. Lee, V. Vimonsatit, and P. Chindaprasirt, "Mechanical and micromechanical properties of alkali
799 activated fly-ash cement based on nano-indentation," *Constr. Build. Mater.*, vol. 107, pp. 95–102,
800 2016.
- 801 [55] H. Lee, V. Vimonsatit, and P. Chindaprasirt, "Mechanical and micromechanical properties of alkali
802 activated fly-ash cement based on nano-indentation," *Constr. Build. Mater.*, vol. 107, pp. 95–102,
803 2016.
- 804 [56] M. Nedeljkovic, Y. Zuo, K. Arbi, and G. Ye, "Natural Carbonation of Alkali-Activated Fly Ash and Slag
805 Pastes," *High Tech Concr. Where Technol. Eng. Meet*, vol. 1, pp. 2213–2223, 2018.
- 806 [57] H. Lee, V. Vimonsatit, P. Chindaprasirt, T. Ngo, and P. Mendis, "Creep properties of cement and
807 alkali activated fly ash materials using nanoindentation technique," *Constr. Build. Mater.*, vol. 168,
808 pp. 547–555, 2018.
- 809 [58] G. Constantinides and F. J. Ulm, "The effect of two types of C-S-H on the elasticity of cement-based
810 materials: Results from nanoindentation and micromechanical modeling," *Cem. Concr. Res.*, vol.
811 34, no. 1, pp. 67–80, 2004.
- 812 [59] Y. Ma, G. Ye, and J. Hu, "Micro-mechanical properties of alkali-activated fly ash evaluated by
813 nanoindentation," *Constr. Build. Mater.*, vol. 147, pp. 407–416, 2017.
- 814 [60] M. Robira, B. Hilloulin, A. Loukili, G. Potin, X. Bourbon, and A. Abdelouas, "Multi-scale investigation
815 of the effect of gamma irradiations on the mechanical properties of cementitious materials," *Constr.*
816 *Build. Mater.*, vol. 186, pp. 484–494, 2018.
- 817 [61] Y. Le Pape, K. G. Field, and I. Remec, "Radiation effects in concrete for nuclear power plants, Part
818 II: Perspective from micromechanical modeling," *Nucl. Eng. Des.*, vol. 282, pp. 126–144, 2015.

- 819 [62] P. Bouniol and E. Bjergbakke, "A comprehensive model to describe radiolytic processes in cement
820 medium," *J. Nucl. Mater.*, vol. 372, no. 1, pp. 1–15, 2008.
- 821 [63] C. A. Rosas-Casarez *et al.*, "Experimental study of XRD, FTIR and TGA techniques in geopolymeric
822 materials," *Int. J. Adv. Comput. Sci. Its Appl.*, vol. 4, no. 4, pp. 25–30., 2014.
- 823 [64] S. A. Bernal *et al.*, "Gel nanostructure in alkali-activated binders based on slag and fly ash, and
824 effects of accelerated carbonation," *Cem. Concr. Res.*, vol. 53, pp. 127–144, 2013.
- 825 [65] A. R. Sakulich, "Characterization of Environmentally-Friendly Alkali Activated Slag Cements and
826 Ancient Building Materials - unpublished thesis," Drexel University, 2009.
- 827 [66] M. Thiery, G. Villain, P. Dangla, and G. Platret, "Investigation of the carbonation front shape on
828 cementitious materials: Effects of the chemical kinetics," *Cem. Concr. Res.*, vol. 37, no. 7, pp. 1047–
829 1058, 2007.
- 830 [67] B. O. Mysen, "The structural behavior of ferric and ferrous iron in aluminosilicate glass near meta-
831 aluminosilicate joins," *Geochim. Cosmochim. Acta*, vol. 70, no. 9, pp. 2337–2353, 2006.
- 832 [68] R. G. Burns, "Mineral Mössbauer spectroscopy: Correlations between chemical shift and quadrupole
833 splitting parameters," *Hyperfine Interact.*, vol. 91, no. 1, pp. 739–745, 1994.
- 834 [69] T. Jurkin, M. Gotić, G. Štefanić, and I. Pucić, "Gamma-irradiation synthesis of iron oxide
835 nanoparticles in the presence of PEO, PVP or CTAB," *Radiat. Phys. Chem.*, vol. 124, pp. 75–83,
836 2016.
- 837 [70] T. I. Sutherland *et al.*, "Effect of ferrous ion concentration on the kinetics of radiation-induced iron-
838 oxide nanoparticle formation and growth," *Phys. Chem. Chem. Phys.*, vol. 19, no. 1, pp. 695–708,
839 2017.
- 840 [71] S. C. Reiff and J. A. Laverne, "Radiation-Induced Chemical Changes to Iron Oxides," *J. Phys. Chem.*
841 *B*, vol. 119, no. 24, pp. 7358–7365, 2015.
- 842 [72] M. Gotić, T. Jurkin, and S. Musić, "Factors that may influence the micro-emulsion synthesis of
843 nanosize magnetite particles," *Colloid Polym. Sci.*, vol. 285, pp. 793–800, 2007.
- 844 [73] J. C. Wren, "Steady-State Radiolysis: Effects of Dissolved Additives," in *Nuclear Energy and the*
845 *Environment*, C. M. Wai and B. J. Minche, Eds. ACS Publications, 2010, pp. 271–295.
- 846 [74] G. Pokrovski *et al.*, "Iron (III)-silica interactions in aqueous solution : Insights from X-ray absorption
847 fine structure spectroscopy," *Geochim. Cosmochim. Acta*, vol. 67, no. 19, pp. 3559–3573, 2013.
- 848 [75] A. Peys, C. E. White, H. Rahier, B. Blanpain, and Y. Pontikes, "Alkali-activation of CaO-FeOx-SiO2
849 slag: Formation mechanism from in-situ X-ray total scattering," 2019.
- 850 [76] J. Am, N. York, and R. August, "Pulse Radiolysis Studies of Alkaline Fe(III) and Fe(VI) Solutions.
851 Observation of Transient Iron Complexes with Intermediate Oxidation States," *J. Am. Chem. Soc.*,
852 vol. 108, no. 3, pp. 523–525, 1986.
- 853 [77] P. Bouniol, "The influence of iron on water radiolysis in cement-based materials," *J. Nucl. Mater.*,
854 vol. 403, no. 1–3, pp. 167–183, 2010.
- 855 [78] W. C. Bray and M. H. Gorin, "Ferryll ion, a compound of tetravalent iron," *J. Am. Chem. Soc.*, vol.
856 54, no. 5, pp. 2124–2125, 1932.
- 857 [79] P. N. Lemougna, K. J. D. Mackenzie, G. N. L. Jameson, and H. R. U. F. Chinje, "The role of iron in
858 the formation of inorganic polymers (geopolymer) from volcanic ash : a ⁵⁷Fe Mössbauer
859 spectroscopy study," *J. Mater. Sci.*, vol. 48, pp. 5280–5286, 2013.
- 860 [80] P. Bouniol, B. Muzeau, and V. Dauvois, "Experimental evidence of the influence of iron on pore water
861 radiolysis in cement-based materials," *J. Nucl. Mater.*, vol. 437, no. 1–3, pp. 208–215, 2013.
- 862